Figure 4.1

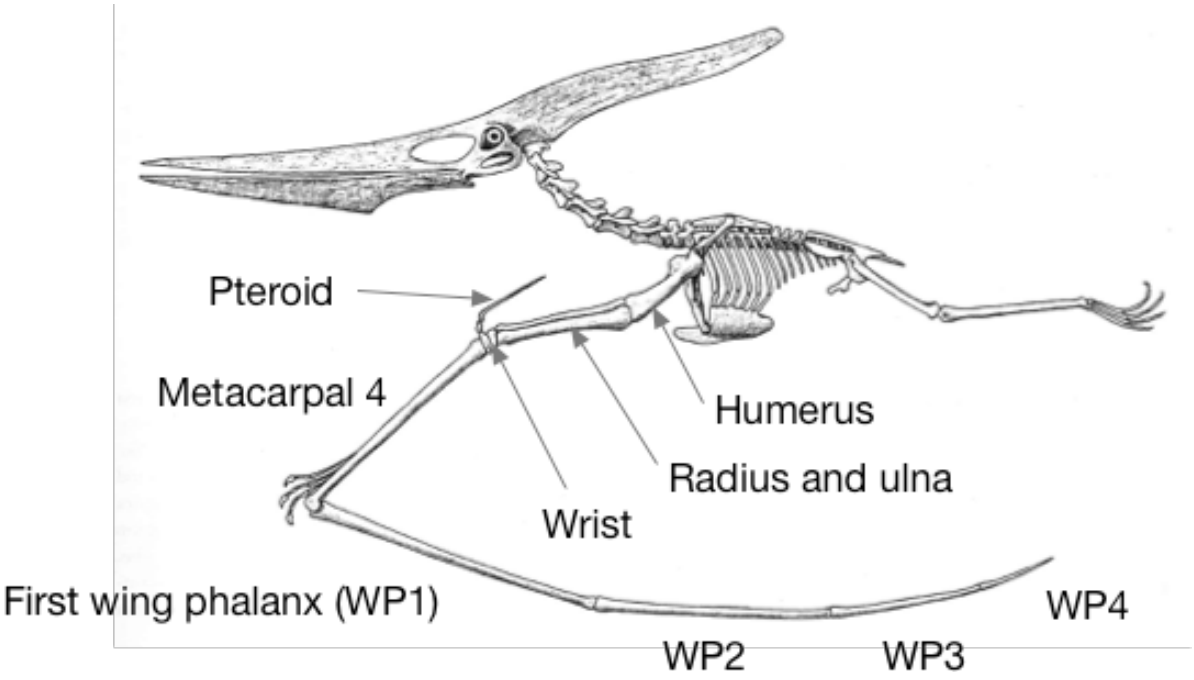

Pteranodon skeletal illustration (adapted from Middleton & English 2014 and Eaton 1910)

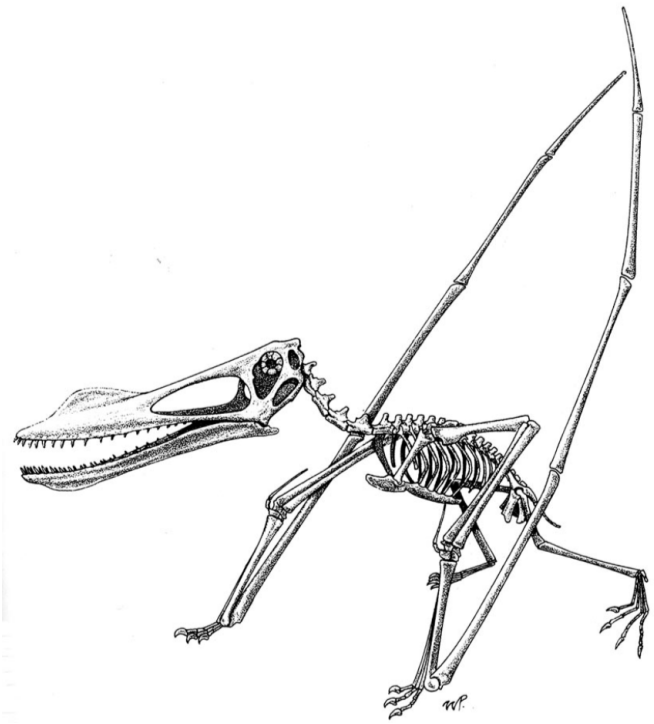

Anhanguera santanae reconstruction showing quadrupedal pose. (Wellnhofer 1988)

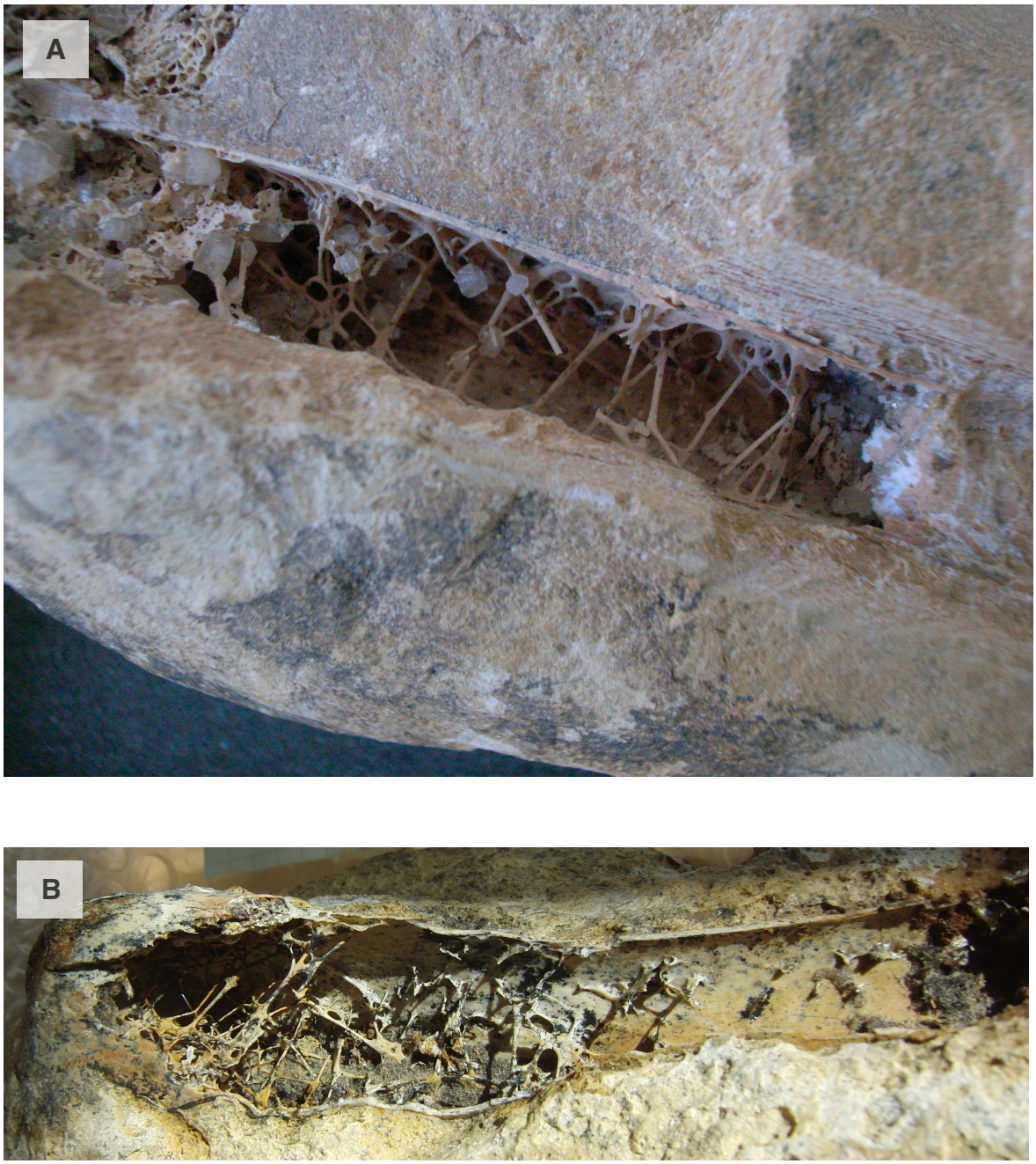

Figure 4.2

Photographs of humerus showing strut like trabeculae ((A) Karlsruhe and (B) Porstmouth specimens, both uncatalogued). Note the diagonal orientation, which is most marked in the lower, Portsmouth specimen.

Figure 4.3

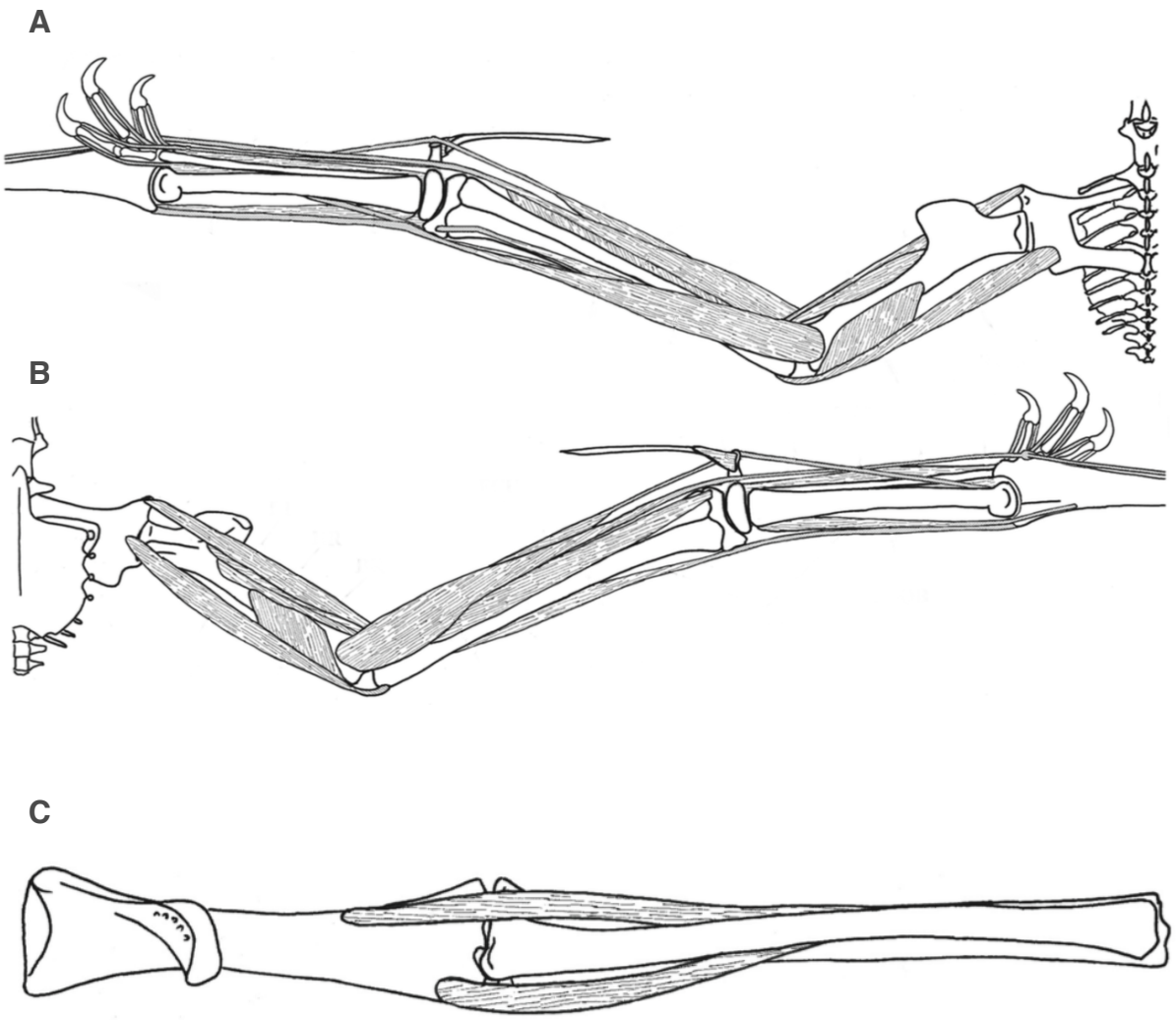

Proximal bones and main muscles of *Anhanguera*. Simplified from Bennett (2008). (A) shows the forelimb in dorsal view and (B) in ventral. It is apparent that the proximal wing bones are surrounded by muscle tissue and tendons, which reduce distally in size and complexity. (C) is an anterior view of the humerus/radius and ulna, showing only the main muscles that span the joint and restrain it dorsoventrally.

Figure 4.4

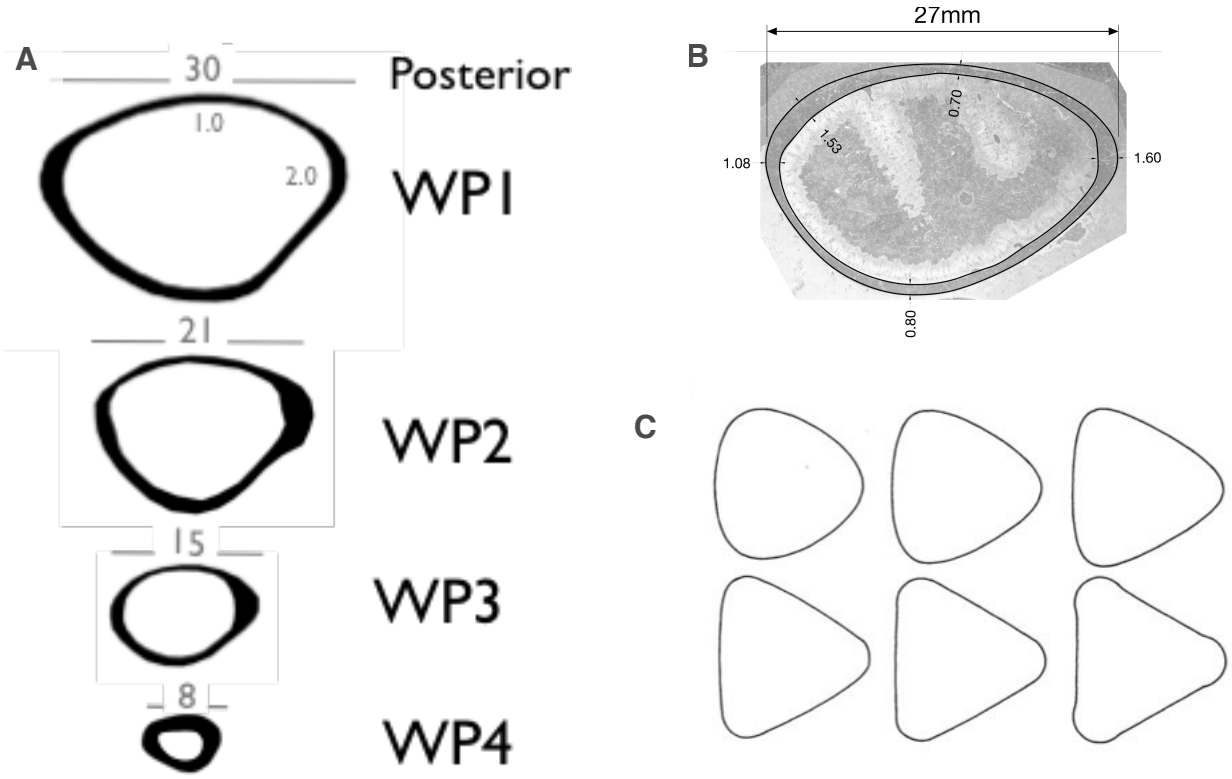

(A) Representative mid shaft wing phalanx cross sections from CT scans and (B) detail from thin section (first wing phalanx from Steel 2005). Dimensions in mm. (C) A selection of structural sections optimised for different combinations of bending and torsional loading (Karihaloo & Hemp 1987). The sub triangular shape is very similar to that of the WP1 and WP2 wing phalanx sections, suggesting a similar loading regime.

Figure 4.5

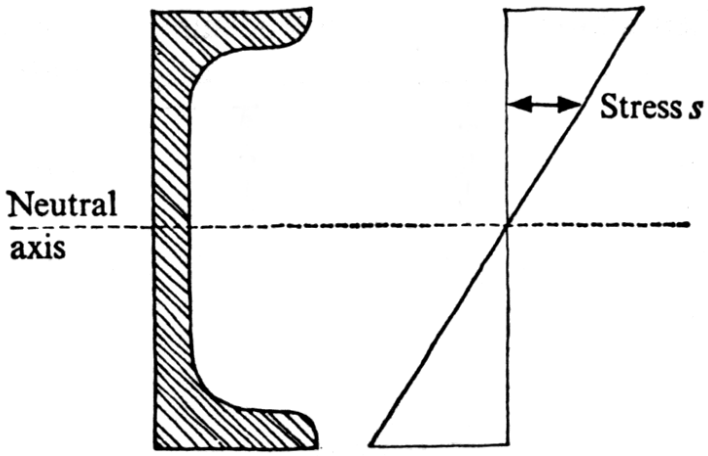

Cross section of a structural section loaded in bending, showing the stress distribution and neutral axis. (From Gordon 1978). Under normal bending in which there is no distortion of the section (a key assumption of beam theory), the stress distribution is linear, regardless of the section shape. The stress is zero at the neutral axis, which passes through the centre of area of the section.

Figure 4.6

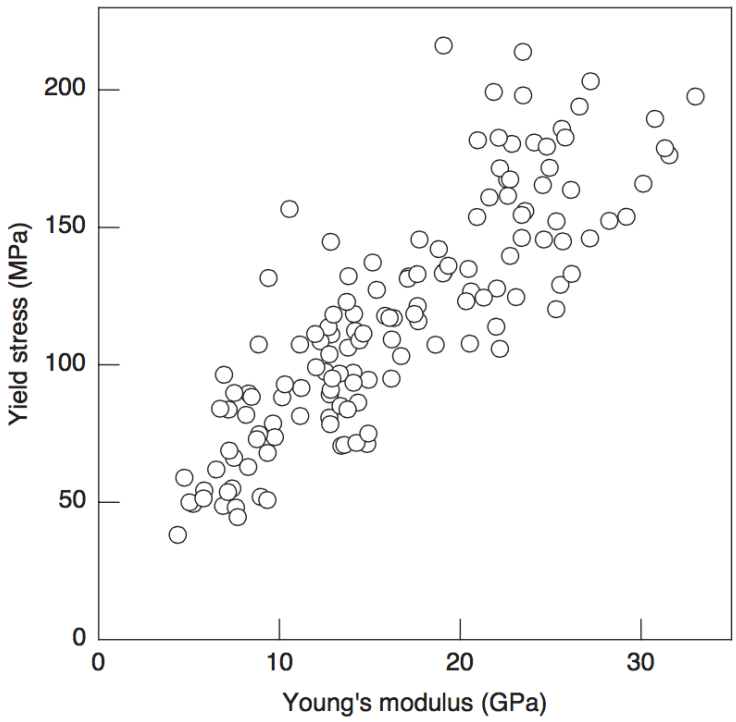

Variation of yield stress with Young's modulus for bone (from Currey 2004). Although there is considerable scatter, there is a broad trend that the yield stress increases with modulus, so strength and stiffness increase together.

Figure 4.7

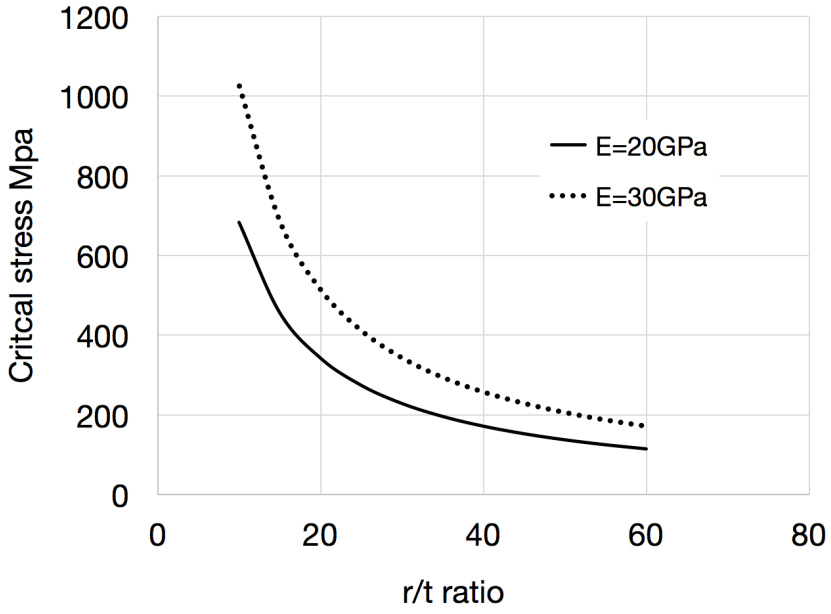

Variation of critical bending stress at which buckling would occur in circular tubes, showing the dependence on the ratio of wall thickness (t) to radius (r) for two values of Young's modulus, applicable to bone.

Figure 4.8

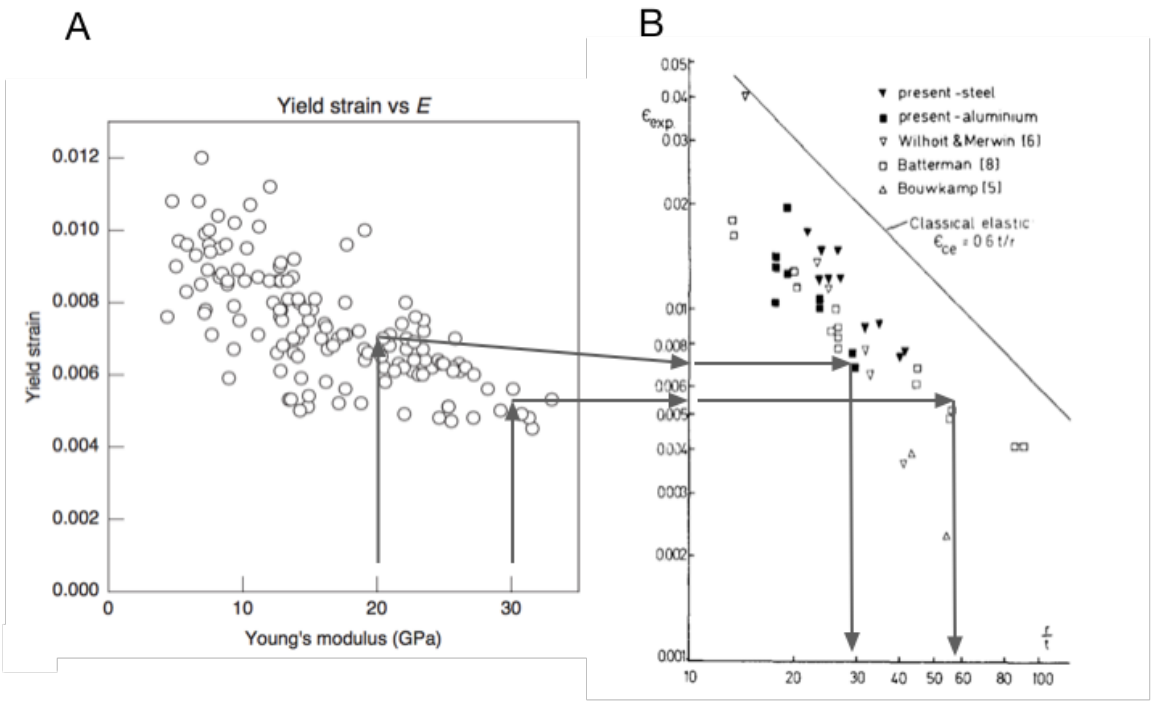

Calculation of critical wall thickness ratios using data from Currey (2004) (A) and Reddy (1979) (B). Graph (A) gives the relationship between yield strain and Young's modulus for bone. Appropriate values are selected for Young's modulus typical of cortical bone and plotted onto the data in (B), to give predictions of the critical r/t values for buckling failure. The result are comparable to those determined from Figure 4.7

Figure 4.9

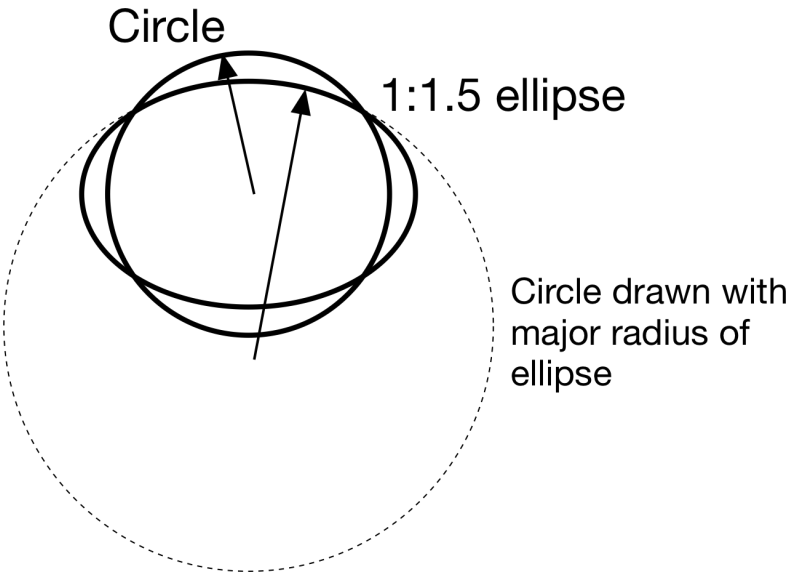

Sketch to illustrate the difference in radius of circle and 1.5:1 ellipse. The radius is almost doubled.

Figure 4.10

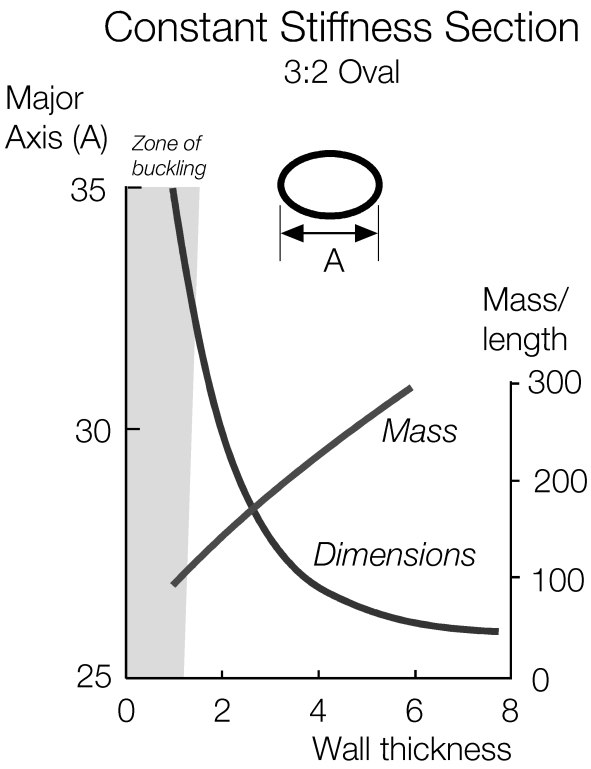

3:2 elliptical section with dimensions adjusted for constant bending stiffness. As wall thickness decreases, the overall dimensions increase. The “j” shaped curve shows this relationship. The diagonal curve is the mass per unit length. As wall thickness decreases and overall dimensions increase, the mass decreases. In practice this is limited by the onset of buckling, shown by the shaded area, which is reached when the r/t ratio approaches 30.

Figure 4.11

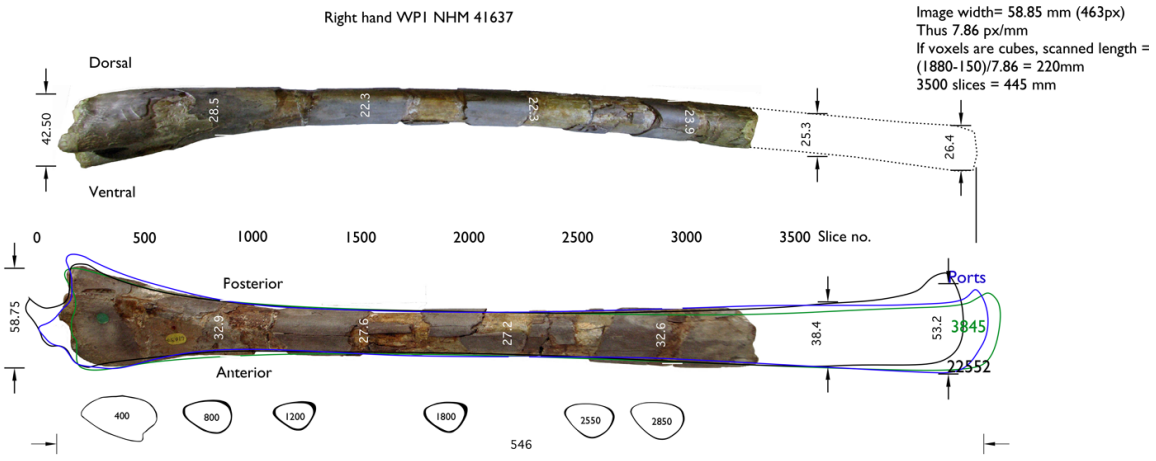

NHMUK PV OR41637 in anterior and dorsal views. Also shown are a selection of cross sections obtained from CT scans and different reconstructions of the distal end of the bone based on other complete specimens. Dimensions in mm.

Figure 4.12

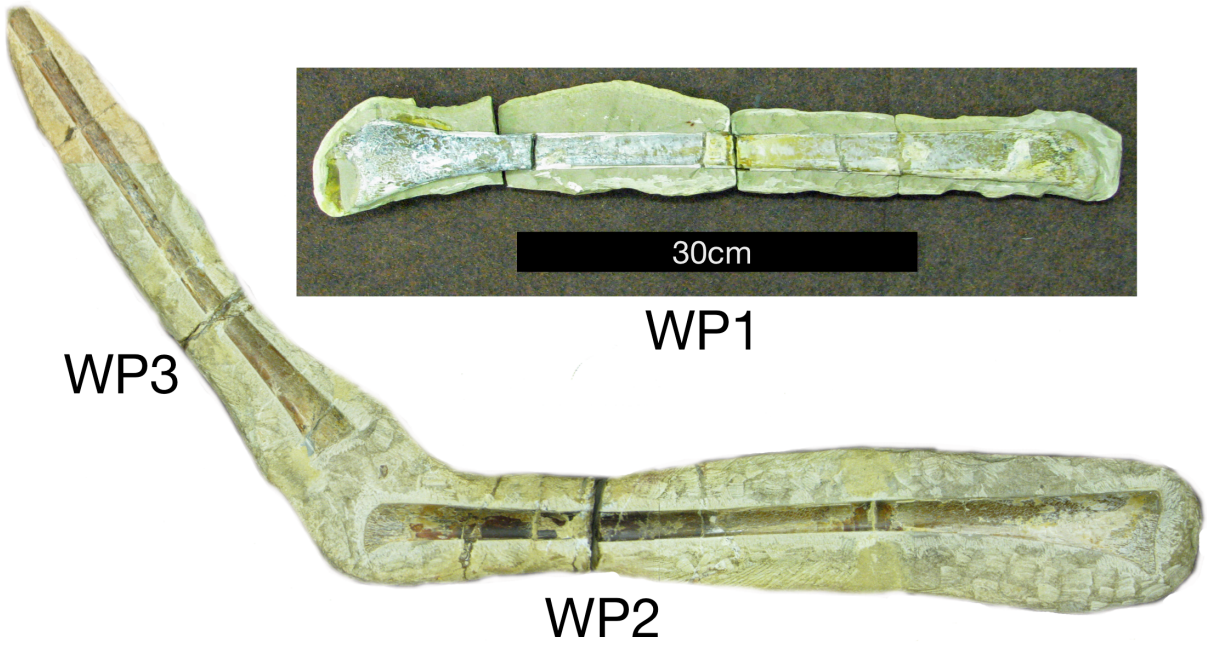

Specimens from the collection held at the University of Portsmouth. They do not have accession numbers, but are known to be from Brazilian cretaceous beds. These specimens were CT scanned at the µ-Viz facility at the University of Southampton.

Figure 4.13

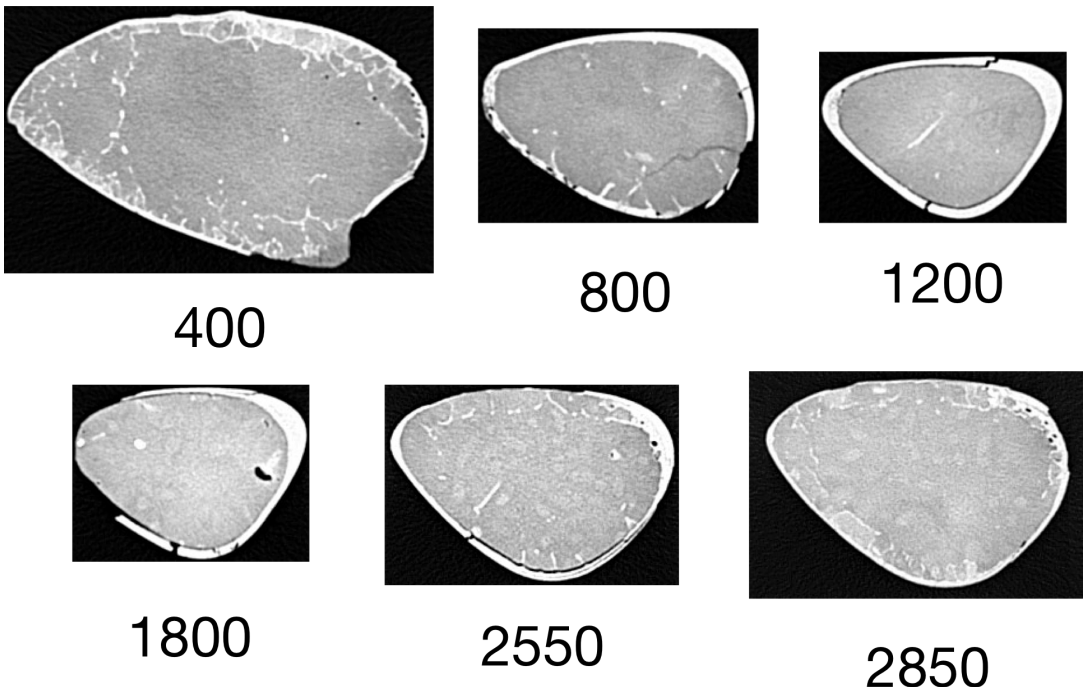

Examples of sections obtained from CT scans (NHMUK PV OR41637 in this case.) Numbers are distance from proximal end in mm.

Figure 4.14

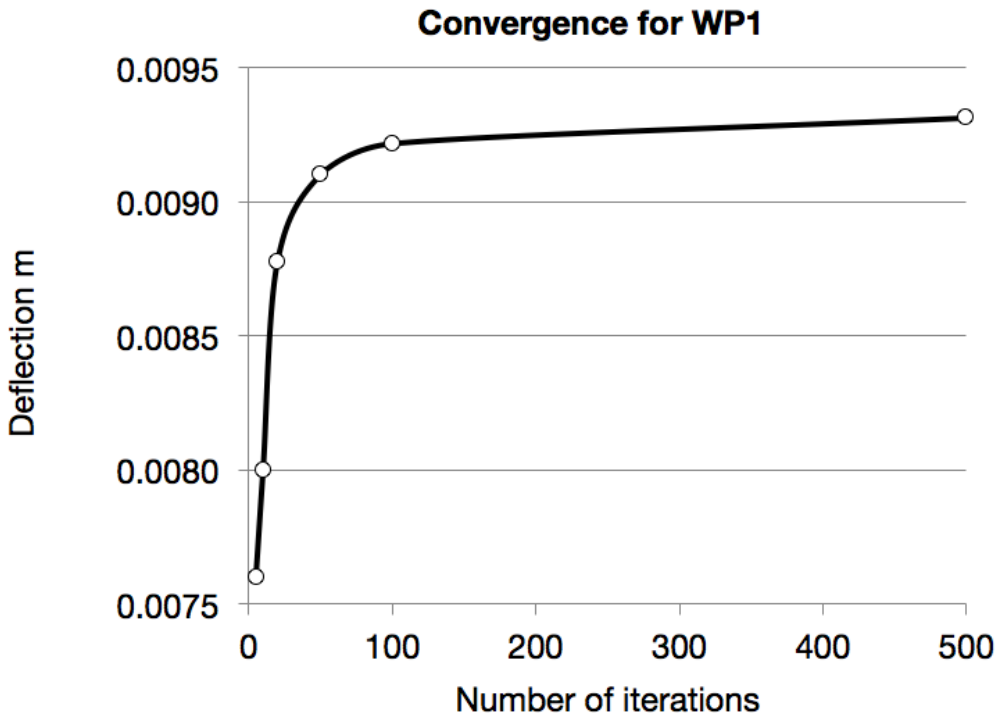

Deflection convergence for beam with WP1 distribution of second moment of area. When compared to asymptotic result for 500 sections, 50 or more sections give better than 2% accuracy.

Figure 4.15

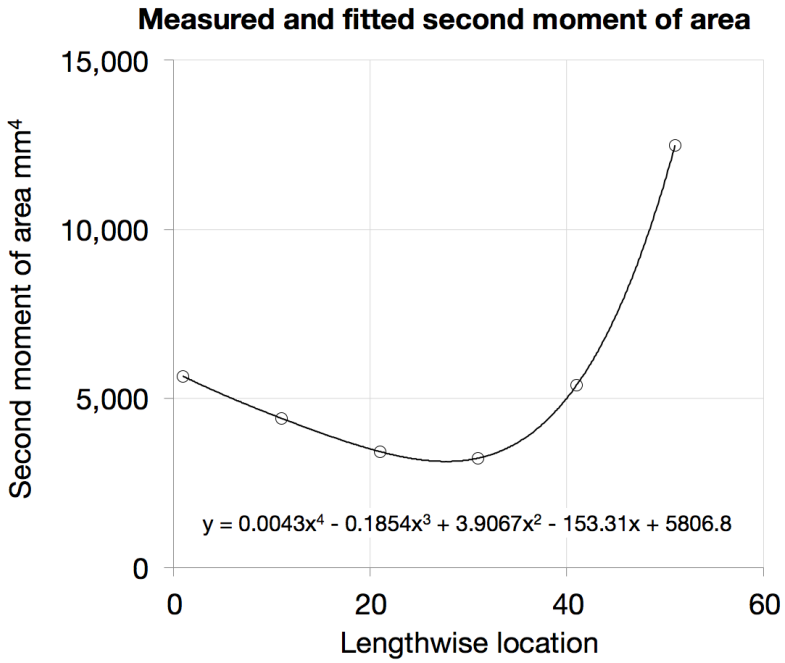

Curve fitting of measured second moment of area used for interpolation of values in the wing spar model. The measured values are shown by circles, the fitted curve by the solid line, with its equation given on the graph.

Figure 4.16

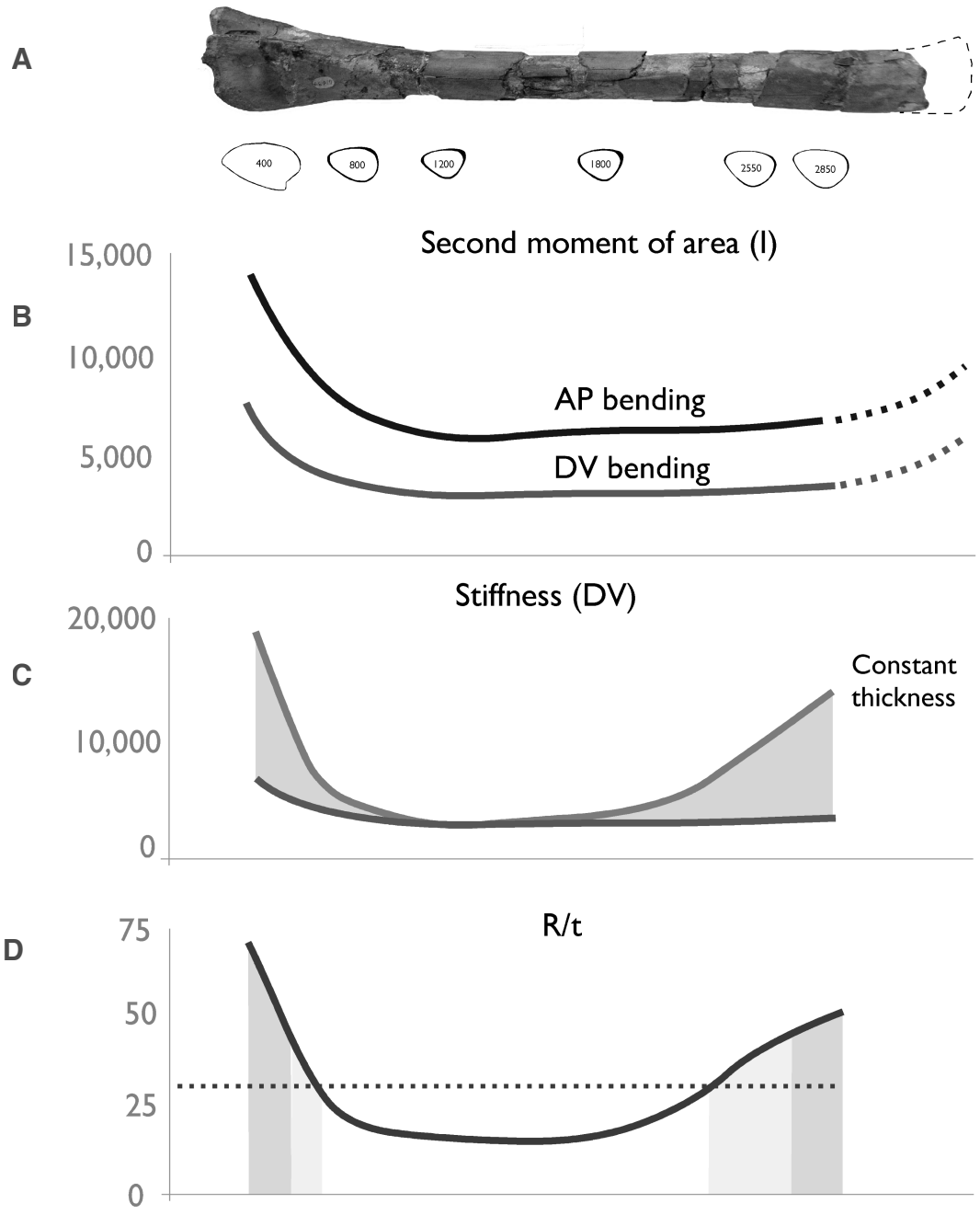

Mechanical properties of NHMUK PV OR41637 deduced from CT scans. (A) WP1 bone and typical sections as in Figure 4.11. (B) Variation of second moment of area along the length. Note approximately 2:1 ratio between DV and AP directions. Units mm^4 (C) Comparison of DV stiffness properties as measured and assuming constant wall thickness, to show the effect of reducing cortical thickness in the epiphyseal regions. (Arbitrary units) (D) Variation of wall thickness ratio. Dotted line is approximate buckling limit. Shaded areas show regions of extensive internal trabecular structures, which coincide with the buckling limit.

Figure 4.17

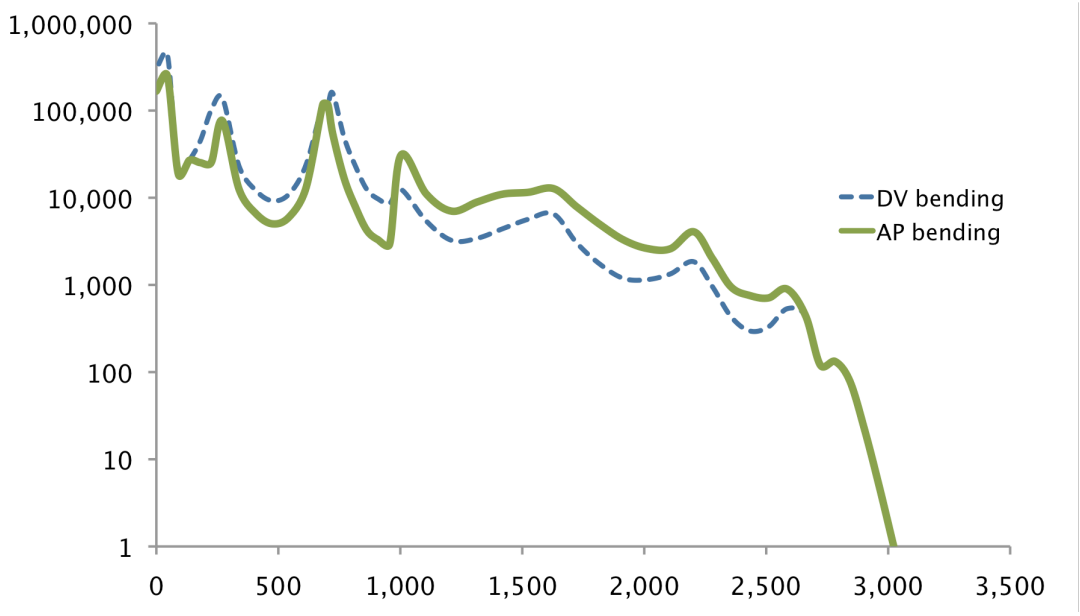

Variation of second moment of area along complete wing spar. Vertical scale is second moment of area (mm^4). Horizontal scale is distance from the proximal end of the humerus, in mm. The joint between the metacarpal and first wing phalanx occurs at approximately 1,000mm. Note that proximal to this joint, the dorsoventral stiffness is greater than the anteroposterior, but this changes in the wing phalanges.